PAPER

Check for updates

Biphasic dissolving microneedles with cyclodextrin inclusion complexes for enhanced delivery of poorly soluble drugs

Runze Wang, [ID] [a] Jiaqi Cao,[a] Jing Zou,[a] Rui Zhang,[a] Mengmeng Li,[a] Wanglong Zhang[a] and Mintong Guo [ID] *[ab]

Dissolving microneedles (DMNs) have been widely investigated for transdermal drug delivery, yet their clinical translation and commercialization remain limited, primarily due to insufficient drug-loading capacity. To address this challenge, we developed a high capacity platform by integrating hydroxypropyl-β-cyclodextrin (HP-β-CD) inclusion technology with a biphasic microneedle design for the delivery of flurbiprofen (FB), a model poorly soluble drug. Comprehensive characterization evaluated the morphology, mechanical strength, and *ex vivo* studies of FB/HP-β-CD DMNs, while *in vivo* pharmacokinetic studies in rats compared their performance with a commercial flurbiprofen gel patch under single- and multiple-dose regimens. The fabricated microneedles exhibited sufficient mechanical strength, with a single needle fracture force of 0.58 ± 0.10 N, adequate for reliable stratum corneum penetration. Each microneedle patch (100 needles) achieved a drug loading of 2.67 ± 0.11 mg, significantly higher than previously reported DMNs. *Ex vivo* permeation studies using a Franz diffusion cell setup using rat skin and phosphate-buffered saline (PBS, pH 7.4) as the receptor medium at 37 °C showed that more than 95% of the drug was released within 24 hours. *In vivo* single-dose studies demonstrated that the DMNs achieved a T_{max} of 2 h, compared to 8 h for the commercial gel patch, and a C_{max} of 124.4 ± 11.4 μg mL^{-1}, resulting in a 2.6-fold increase in bioavailability (AUC$_{0 \to 24h}$ of 1247.6 ± 240.7 μg h mL^{-1} for DMNs *versus* 485.0 ± 63.0 μg h mL^{-1} for the commercial gel patch). Multiple-dose studies confirmed flexible modulation of the pharmacokinetic profile by adjusting dosing frequency. In conclusion, the FB/HP-β-CD inclusion biphasic DMN system offers an effective approach for transdermal delivery of poorly soluble drugs.

1. Introduction

Microneedle (MN) technology, first proposed by Henry in 1998,[1] has since evolved to various types, such as hollow, solid, coated, dissolving, and hydrogel microneedles.[2–6] These systems mechanically puncture the stratum corneum to form microchannels, enabling painless and minimally invasive transdermal drug delivery with advantages such as rapid onset of action, enhanced bioavailability, and high patient compliance. Among them, dissolving microneedles (DMNs) have attracted particular attention due to their minimal invasiveness and rapid dissolution in the skin, and demonstrated efficacy in delivering vaccines and other therapeutics.[7–9] However, most previous studies have focused on macromolecules with low loading dose requirement or small molecules with high

solubility.[10–12] Drug-loading strategies for poorly soluble drugs remain largely unexplored.

A major challenge in the clinical translation of DMNs is their insufficient drug-loading capacity.[7] Depending on the needle height, array density, and geometry, the calculated physical drug capacity of a single microneedle is typically very small, ranging from 1 to 20 nL. Even for a patch of 100 microneedles with an area of 1 cm^2, the total drug loading volume is only 1–20 μL.[13,14] Achieving milligram-level dosing in this limited space requires drug concentrations exceeding 50–100 mg mL^{-1}, which is impractical for most poorly soluble drugs due to their low aqueous solubility.[15] Yerneni *et al.* developed microneedles for the delivery of extracellular vesicle-encapsulated curcumin, which reached a drug loading of ∼0.05 mg cm^{-2}, likely below the effective dose for clinically relevant applications.[16] In the case of insulin microneedles, Cao *et al.* reported a drug loading of ∼3.5 μg per needle, making the total drug content of the entire microneedle patch insufficient for clinical dose requirements.[17,18] To improve drug loading, Qin *et al.* utilized a drug-loaded nanoparticle-microneedle composite system to increase paclitaxel loading.[19] Similarly, Yao *et al.* described the

[a]School of Pharmaceutical Sciences, Zhengzhou University, Zhengzhou, Henan, China. E-mail: guo5566@126.com

[b]Pingyuan Laboratory, State Key Laboratory of Antiviral Drugs, Xinxiang, Henan, China

advantages of combining nanoformulations with DMN technology to facilitate the delivery of a wide range of drugs.[20] However, the complexity of nano drug preparation process likely raises production costs for large-scale manufacturing of these delivery systems. Moreover, the stability of nanoparticles during microneedle drying stage remains a major challenge. Collectively, these studies highlight the need for new strategies beyond excipient modifications or formulation adjustments to solve the drug solubility and loading problems.

To address the challenges of limited loading capacity while improving delivery efficiency, the design of biphasic dissolving microneedle has been developed. In this structure, drug-containing water-soluble microneedle tips are mounted on an insoluble backing layer. After application, the tips dissolve and deliver the drug into the skin, while the backing layer prevents drug migration or diffusion into the backing during fabrication and application.[21,22] This design improves drug delivery efficiency and reduces residual drug on the patch after removal, thereby alleviating, to some extent, the clinical translation bottleneck posed by inadequate loading capacity. Nevertheless, biphasic designs still require high drug solubility within the tip matrix, underscoring the need for complementary strategies such as cyclodextrin inclusion complexes to further enhance loading of poorly soluble compounds.

Another critical issue hindering commercialization of most DMNs is the lack of key pharmacokinetic data to support their clinical translation.[23] Specifically, the pharmacokinetic parameters of microneedle-mediated drug delivery have not been consistently compared to existing standard therapies. For example, the pharmacokinetics of metformin delivered by DMNs was compared to subcutaneous injection but not to the oral route,[24] the most common method of drug administration, making it difficult to assess their clinical replacement potential. Similarly, the characterization of *in vivo* absorption of diclofenac DMNs has not been compared directly with approved topical gels in terms of local tissue concentrations, time of onset, and analgesic duration, leading to unclear product positioning.[25] The lack of studies comparing microneedles with existing formulations has limited the translation of DMNs into clinic and ultimately hinders their path to commercialization.[26]

This study uses flurbiprofen (FB, solubility < 10 μg mL^{-1}), a poorly soluble small molecule drug, as a proof of concept to validate a dual-phase DMN system based on drug inclusion complexes. This system significantly improves the solubility of FB through the use of hydroxypropyl-β-cyclodextrin (HP-β-CD) inclusion. Combining with biphasic DMN structure with sufficient mechanical strength, this new system concentrates the drug in the needle tip region, thus achieving high drug loading and high delivery efficiency. In addition, we conducted systematic *ex vivo* permeation studies and pharmacokinetic measurements in rats using the commercially available FB gel as a control formulation. By comparing key pharmacokinetic parameters such as T_{max}, C_{max}, and AUC, we validated the rapid onset and enhanced bioavailability of the dual-phase FB/HP-β-CD DMNs. This study not only provides a novel technical solution for the transdermal delivery of poorly soluble drugs but

also offers pharmacokinetics data supporting future clinical translation and commercialization.

2. Materials and methods

2.1. Materials

Flurbiprofen and ketoprofen were obtained from Hunan Jiudian Hongyang Pharmaceutical (Hunan, China). Hydroxypropyl-β-cyclodextrin (HP-β-CD) was purchased from Fuyang Tianli Pharmaceutical Excipients (Fuyang, China). Polyvinyl alcohol (PVA 05-88) and hydroxypropyl methylcellulose (HPMC E5) were acquired from Jiangxi Alpha High-tech Pharmaceutical (Jiangxi, China). Polyvinylpyrrolidone (PVP K90) was sourced from BASF (Germany). Chondroitin sulfate (CS) was supplied by Hunan Wuxing Biotechnology (Hunan, China). Polyurethane acrylate (PUA-Cure 9110), hydroxypropyl methacrylate (HPMA), and photoinitiator (2,4,6-trimethylbenzoyl) diphenylphosphine oxide (TPO) were provided by Kunshan Caste Polymer Material (Jiangsu, China) and Sigma-Aldrich (USA). Parafilm M® was obtained from Bemis Company (USA). Pre-treated porcine skin was supplied by Muyuan Food (Henan, China). Microneedle PDMS molds (array 10 × 10, needle height 780 μm, needle base size 1 cm × 1 cm) were acquired from Taizhou Microchip Medical Technology (Zhejiang, China). The flurbiprofen gel patch was provided by Beijing Tide Pharmaceutical (Beijing, China).

SD rats (male, 6–8 weeks old, weight 270 ± 10 g) were provided by Spaflor (Beijing) Biotechnology Co., Ltd. The animal experiments were conducted under the permission of the Animal Ethics Committee of Zhengzhou University of Pharmaceutical Sciences (Zhengzhou, China) (permission number SCXK2024-0001). All animal experiments involved in this study complied with the ARRIVE guidelines. Furthermore, all procedures were performed in accordance with relevant national and institutional guidelines for the care and use of animals in research, ensuring compliance with ethical standards and regulations for animal welfare.

2.2. Analysis of flurbiprofen content

The flurbiprofen content was determined by high-performance liquid chromatography (HPLC, Agilent 1200 series) equipped with an Eclipse XDB-C18 column (4.6 mm × 150 mm, 5 μm). The mobile phase was consisted of methanol, deionized water, and glacial acetic acid in a ratio of 65 : 30 : 5 (v/v/v). The injection volume was 10 μL and the flow rate was set at 1.0 mL min^{-1}. Detection was performed at 247 nm. The column temperature was maintained at 35 °C. The limit of detection (LOD) and limit of quantification (LOQ) were 0.2 μg mL^{-1} and 0.6 μg mL^{-1}, respectively.

2.3. Preparation of inclusion complexes

2.3.1. Determination of phase solubility. The phase solubility method reported by Higuchi and Connors was employed to determine the equilibrium constant and inclusion ratio of the inclusion complex.[27] HP-β-CD aqueous solutions with the concentrations of 0, 1, 2, 4, 6, 8, and 10 mmol L^{-1} were prepared

in 10 mL of deionized water. Excess amount of solid FB was then added to the HP-β-CD solution and mixed with shaking at 120 rpm and 25 °C for 72 h. Saturation was assumed when excess FB solids remained visible at the bottom of the container after thorough mixing and equilibration for a sufficient period. Under these conditions, the measured concentration was considered to represent the maximum solubility of the drug in the experimental medium. After the equilibrium was reached, the FB content in the HP-β-CD solution was measured by HPLC according to method 2.2. The molar concentrations of FB were calculated and plotted against the molar concentrations of HP-β-CD to construct a phase solubility curve. The equilibrium constant of FB/HP-β-CD was calculated according to the following eqn (1):[28]

$$K_S = \frac{\text{slope}}{S_0 \times (1 - \text{slope})} \qquad (1)$$

where slope represents the slope of the phase solubility curve, S_0 is the intrinsic solubility of FB in water in the absence of cyclodextrin (mmol L^{-1}), and K_S is the apparent stability constant (M^{-1}).

2.3.2. Preparation of inclusion complexes. The FB/HP-β-CD inclusion complexes were prepared by freeze-drying, adapting from previously reported procedures with minor modifications.[29] The effects of the molar ratio, stirring temperature, and stirring time on the complex formation were investigated (SI Table S1). A three-factor, three-level orthogonal experimental design was then employed to optimize the preparation conditions, as presented in SI Table S2. HP-β-CD and FB were weighed according to the orthogonal experimental design for different molar ratios. FB was dissolved in a 15% (w/w) aqueous solution of HP-β-CD with stirring at different temperature and stirring time. After the solution reaching room temperature, it was filtered through a 0.45 μm polyethersulfone (PES) membrane to remove any undissolved FB, ensuring the FB/HP-β-CD complexes in solution were retained.[30] The filtrate was frozen at −40 °C for 14 h and then lyophilized for 48 h to obtain the inclusion complex powder. The powder was weighed, dissolved in methanol, and sonicated for 20 min to release the encapsulated FB for drug content analysis (Section 2.2). The drug loading (S_1, %) and encapsulation efficiency (S_2, %) were calculated, and the evaluation index S was determined by eqn (2) and (3): $S = 30\% \times S_1 + 70\% \times S_2$.

$$\%S_1 = \frac{\text{Amount of drug in inclusion complex}}{\text{Weight of inclusion complex}} \times 100\% \qquad (2)$$

$$\%S_2 = \frac{\text{Mass of reactant transformed}}{\text{Initial mass of reactant}} \times 100\% \qquad (3)$$

2.4. Characterization of inclusion complexes

2.4.1. DSC. The thermal properties of FB, HP-β-CD, a physical mixture of FB and HP-β-CD, and FB/HP-β-CD inclusion complex powder were analyzed using differential scanning calorimetry (DSC 204 F1Phoenix, NETZSCH, Germany). Samples (approximately 10 mg each) were placed in aluminum crucibles

and a blank aluminum crucible was used as reference. The temperature was increased from 30 to 400 °C at a heating rate of 10 °C min⁻¹ under nitrogen with a flow rate of 20 mL min⁻¹.

2.4.2. XRD. The crystallinity of FB, HP-β-CD, a physical mixture of FB and HP-β-CD, and FB/HP-β-CD inclusion complex powder was measured using X-ray diffraction (XRD, Smart Lab SE, Rigaku, Japan). Samples were placed in aluminum containers and scanned over a 2θ range of 10° to 60° at a scanning rate of 2°/min. All measurements were performed at room temperature.

2.4.3. FT-IR. Fourier transform infrared spectroscopy (FT-IR, NICOLET iS10, Thermo Fisher Scientific, USA) was used to determine the chemical structure of FB, HP-β-CD, a physical mixture of FB and HP-β-CD, and FB/HP-β-CD inclusion complex powder. Samples were mixed with potassium bromide (KBr) at a ratio of 1 : 100 (w/w) and pressed into transparent pellets. Spectra were recorded in the range of 4000 to 400 cm⁻¹ with a resolution of 4 cm⁻¹.

2.5. Fabrication of biphasic DMNs loaded with inclusion complexes

The formulations of DMN tips and the backing are shown in Table 1 and SI Table S3. To prepare the microneedle tips, FB/HP-β-CD and PVP, PVA, CS, and HPMC E5 were each dissolved separately in purified water. The solutions were stirred until homogeneous, followed by vacuum aspiration (0.08 MPa, 2 min) to remove excess solution from the mold of microneedle tips. The molds were then placed in a drying chamber at room temperature for 12 h.

For the backing solution, the compounds listed in SI Table S3 were stirred in the dark for 30 min and allowed to stand for 2 h to remove air bubbles.[31] After the microneedle tips had dried, the backing solution was added, followed by centrifugation at 4000 rpm for 2 min. The microneedles were then cured by UV exposure ($\lambda = 365$ nm, 180 W) for 3, which promotes the solidification of the insoluble backing, shortens the overall microneedle fabrication time, and subsequently demolded. The structural and functional differences between conventional dissolving microneedles and the biphasic system is presented in SI Fig. S2. The stepwise fabrication process of the biphasic dissolving microneedles is schematically illustrated in SI Fig. S3.

2.6. Characterization of biphasic DMNs

2.6.1. SEM. The surface morphology of the fabricated microneedles was characterized using scanning electron microscopy (SEM, Gemini 300, Carl Zeiss, Germany). Prior to imaging, the microneedles were sputter-coated with a thin layer of gold to enhance conductivity and fixed onto a sample holder. The samples were examined at an accelerating voltage of 5 kV, and images were acquired at magnifications of 30×, 50×, and 100×.

2.6.2. Confocal microscopy. The distribution of drugs within the microneedles was evaluated using confocal microscopy (AI series, Nikon, Japan). Rhodamine B (RhB, 2.7%), a red fluorescence dye, was loaded into the tips, while Coumarin-6 (Cou-6), a green fluorescence dye, was incorporated into the

Table 1 Formulations of the microneedle tips used for the fabrication of biphasic inclusion complex DMNs

Formula	FB/HP-CD (g)	PVP K90 (g)	PVA 05-88 (g)	CS (g)	HPMC E5 (g)	Water (g)
F1	1.500	0.050				1.000
F2	1.500		0.050			1.000
F3	1.500			0.050		1.000
F4	1.500				0.050	1.000

backing. Four microneedles (2 × 2 array) were carefully cut, and the bottom of microneedles were glued to a glass slide using soybean oil. During the scanning, the microneedle tip and backing were designated as the "Top" and "Bottom" surface, respectively. The fluorescence signals of RhB and Cou-6 were detected at 570 nm and 480 nm, respectively. Three-dimensional (3D) images were reconstructed from z-stack scans acquired at 25 μm intervals, covering the region from the backing to the tip of the microneedles.

2.6.3. Mechanical strength tests. The mechanical strength of the microneedles was evaluated using a texture analyzer (TA.HDplus, Stable Micro Systems, UK). Microneedle patches were cut into a 3 × 3 array (9 microneedles). The microneedles were placed on the platform of a texture analyzer with the tips facing up. Under the compression mode, the probe was slowly moved downward at a constant speed, with the pre- and post-compression speed set at 1 mm s^{-1} and the testing speed at 0.1 mm s^{-1}. Tests for each group were conducted in triplicates. Force-displacement curves were generated and the force each microneedle could withstand was calculated accordingly.

A Parafilm insertion test was conducted, since Parafilm is widely employed as a skin simulant to assess microneedle insertion efficiency.[32] Parafilm sheets were cut into 1.5 × 1.5 cm squares, folded into eight layers (127 μm per layer), and microneedle patches were pressed onto the stack using a 4 N weight for 2 min. The number of layers penetrated by each microneedle was observed under a stereomicroscope, and the insertion rate for each layer was calculated.

2.6.4. Determine flurbiprofen content in microneedle tips. The microneedle tips were physically separated from the base layer using a surgical blade, following a previously reported method.[33] The collected tips and the remaining base layer were dissolved separately in methanol, sonicated for 20 min, centrifuged, and filtered through a 0.22 μm membrane prior to HPLC analysis (Section 2.2). Flurbiprofen content in each fraction was quantified from the calibration curve, and drug loading per patch was expressed as mean ± S.D. (n = 3).

2.6.5. Histology analysis of skin tissue. To investigate the skin penetration capability of biphasic DMNs, the DMN patches were pressed onto the shaved back of rats for 2 min. After microneedle application, the treated skin areas were excised and immediately fixed in 10% formalin. The samples were then paraffin-embedded and sectioned at 10 μm thickness.[34] The sections were stained with hematoxylin and eosin (H&E) and examined under a light microscope to evaluate microneedle-induced microchannels and overall tissue morphology.

2.7. *Ex vivo* skin permeation

The *ex vivo* transdermal delivery of FB from biphasic DMNs was evaluated using excised rat dorsal skin mounted on Franz diffusion cells. The microneedle patches were vertically applied onto the skin with a 4 N force for 2 min to ensure complete insertion. This force was applied quantitatively using a standard weight (approximately 408 g) with a flat bottom surface of 1.5 cm in diameter, slightly larger than the 1 cm × 1 cm microneedle patch, to achieve uniform pressure across the patch area.

After insertion, the treated rat skin was mounted onto Franz diffusion cells with the stratum corneum facing the donor compartment. The receptor compartment was filled with phosphate-buffered saline (PBS, pH 7.4), maintained at 37 ± 0.5 °C using a circulating water bath, and stirred continuously at 100 rpm. At predetermined time points (0, 0.25, 0.5, 1, 2, 4, 6, 8, 12, and 24 h), 3 mL of receptor fluid was withdrawn, filtered, and analyzed for FB content, with an equal volume of fresh PBS replenished after each sampling. PBS (pH 7.4) was selected as the receptor fluid to maintain sink conditions, as flurbiprofen's saturation solubility in this medium (approximately 4.22 mg mL^{-1}) far exceeds the maximum receptor concentration achieved (approximately 0.18 mg mL^{-1} after 95% permeation). The cumulative permeation percentage was calculated as previously described.[35] To quantitatively evaluate transdermal drug delivery, the cumulative permeation percentage (P_t) was calculated using the following eqn (4):

$$P_t = \frac{C_t V + \sum_{i=1}^{n-1} C_i V_s}{A D_0} \quad (4)$$

where C_t is the drug concentration at time t (μg mL^{-1}), C_i is the concentration of each previous sample, V is the receptor volume (mL), V_s is the sample volume (mL), A is the an effective diffusion area (cm^2), and D_0 is the initial drug loading per unit area of the patch (μg cm^{-2}).

2.8. *In vivo* pharmacokinetics

2.8.1. Dosage and blood sampling. The *in vivo* pharmacokinetic profile of FB/HP-β-CD biphasic DMNs was determined and compared to that of commercial flurbiprofen gel patches in rats. Prior to the experiment, rats were shaved on the back and fasted for 12 h. In the biphasic DMN group, a 4 N force was applied for 2 min to facilitate the insertion of microneedles into the skin and followed by the removal of the backing layer. In the gel patch group, the patch was applied to the back skin and secured with medical tape to prevent displacement. Blood

Table 2 Single dose administration dosage table

Group	Drug content (mg)	Dose (mg kg^{-1})
F4 MN	5.56 mg	20.6
FB cataplasms	0.29 mg cm^{-2} (4.8 cm × 4 cm, 19.2 cm^2)	20.6

samples (0.3 mL) were collected *via* the orbital vein at 0.25, 0.5, 1, 1.5, 2, 3, 4, 6, 8, 12, 24, 36, and 48 h after a single dose. The dose regimen is provided in Table 2.

In the multiple-dose study, dosing intervals of 12 and 24 h with six consecutive doses were evaluated. For the 12 h interval, blood samples were collected at 0, 0.5, 1, 2, 4, 6, 8, and 12 h after the first dose; 0.5, 1, 2, 6, and 12 h after the second dose; 1, 2, 6, and 12 h after the third to fifth doses; and 12 h before the final dose, as well as 0, 1, 2, 4, 6, 8, 12, 24, and 48 h after the final dose. For the 24 h interval, samples were taken at 0, 0.5, 1, 2, 4, 6, 8, 12, and 24 h after the first dose; 0.5, 1, 2, 4, 6, 12, and 24 h after the second dose; 1, 2, 4, 6, 12, and 24 h after the third to fifth doses; and 24 h before the final dose, as well as 0, 1, 2, 4, 6, 12, 24, 36, and 48 h after the final dose.

2.8.2. Detection of flurbiprofen in plasma samples. Blood samples collected from the orbital vein of rats were placed into 1.5 mL anticoagulant tubes. The samples were centrifuged at 4000 rpm for 10 min at 4 °C to obtain plasma. The plasma samples were stored at −20 °C until the time of the measurement. For the detection of flurbiprofen by HPLC, an aliquot of 50 μL of plasma sample was combined with 50 μL of internal standard and 200 μL of methanol, vortexed for 1 min, and centrifuged at 13 000 rpm for 5 min. The supernatant was transferred to a 1.5 mL microcentrifuge tube and centrifuged again at 13 000 rpm for 5 minutes. After the second centrifugation, the supernatant was used for the measurement of flurbiprofen content according to method 2.2. Ketoprofen was used as the internal standard (20 μg mL^{-1}). The ratio of flurbiprofen concentration over internal standard (X) was plotted against the peak area ratio of flurbiprofen over internal standard (Y). A linear relationship was observed between flurbiprofen concentration and peak area in the range of 1–150 μg mL^{-1}, with the regression equation of $y = 0.1455x + 0.5657$ ($R^2 = 0.9992$). The pharmacokinetic parameters, including T_{max}, C_{max}, and $AUC_{0 \to 24h}$, for both the microneedle and gel patch administration routes were calculated using Phoenix WinNonlin 8.3 software.

2.9. Statistical analysis

Data were analyzed using Excel and Origin 2024 software. Statistical significance was assessed using one-way analysis of variance (ANOVA). A *p*-value of less than 0.05 was considered statistically significant.

3. Results and discussion

3.1. Preparation and characterization of inclusion complexes

To increase the solubility of FB, we prepared FB/HP-β-CD inclusion complexes using increasing concentrations of HP-β-CD. The phase-solubility studies showed a linear increase in the solubility of FB as the concentration of HP-β-CD increases. The phase-solubility curve (SI Fig. S1) followed an A_L-type model[36] ($Y = 0.2987X + 0.1001$, $R^2 = 0.9990$), indicating a 1 : 1 molar ration of FB and HP-β-CD in the complex. The calculated solubility constant (K_S)[37] was 4255 L mol^{-1}, with K values ranging between 200 and 5000 L mol^{-1}, suggesting a stable complex.[38] The initial solubility of FB was 0.100 mmol L^{-1} (equal to 0.0315 mg mL^{-1}), which was increased to 3.09 mmol L^{-1} (0.970 mg mL^{-1}) after forming complex with HP-β-CD, corresponding to an approximate 30-fold increase in solubility. Consistent with previous reports, our results confirmed that cyclodextrin-based inclusion complexes can improve the solubility of poorly soluble drugs.[39,40]

Furthermore, the range analysis (SI Tables S2 and S5) showed that the molar ratio of FB to HP-β-CD has the largest effect on the formation of inclusion complexes compared to other factors such as temperature and time. The effect exerted by the molar ratio was statistically significant ($F = 21.227$, $P < 0.05$), whereas the effect of temperature and time was not. Based on these results, we selected the molar ratio of 1 : 1, the preparation temperature of 60 °C, and the stirring time of 6 h as the condition for preparing the FB/HP-β-CD inclusion complex. Following this condition, we were able to achieve the yield of 94.32 ± 0.42%, the encapsulation efficiency of 80.48 ± 1.27%, and the drug load of 40.00 ± 0.69% in the production of three separate batches of these inclusion complexes. The resulting FB/HP-β-CD inclusion complex exhibited a saturated solubility in water of 2.30 ± 0.13 g mL^{-1}, expressed as the concentration of the inclusion complex in solution.

We next conducted DSC, XRD and FT-IR experiments to characterize the biophysical properties of FB/HP-β-CD inclusion complex. As shown by DSC analysis, FB exhibited a prominent peak at 111.2 °C indicating the melting point of its crystalline structure [Fig. 1A(a)]. On the other hand, HP-β-CD remained stable as no DSC peak was observed within the temperature range [Fig. 1A(b)]. In the physical mixture, the DSC signature for FB and HP-β-CD remained unchanged [Fig. 1A(c)]. However, the FB peak disappeared in the FB/HP-β-CD inclusion complex, suggesting that embedding of FB into the cavity of HP-β-CD likely disrupts its crystalline structure to produce a thermal stable complex [Fig. 1A(d)]. Similarly, the characteristic diffraction peaks of FB observed by XRD analysis completely disappeared in the inclusion complex, further confirming the loss of FB crystalline structure [Fig. 1B(d)]. Furthermore, FT-IR spectroscopy revealed shifts in the characteristic absorption peaks of FB within the complex [comparing Fig. 1C(a) and (d)]. Collectively, these results confirmed that stable FB/HP-β-CD inclusion complexes produced in our study are formed through molecular embedding and hydrogen bond interactions.
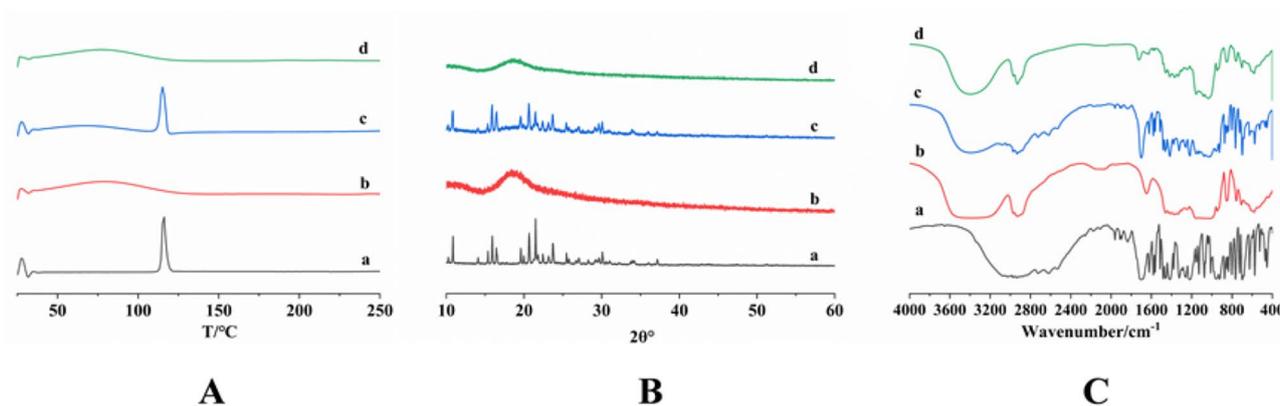
Fig. 1 Biophysical characterization of FB/HP-β-CD inclusion complexes. (A) DSC, (B) XRD, (C) FT-IR analyses of FB (a), HP-β-CD (b), a physical mixture of FB and HP-β-CD at 1 : 1 ratio (c), and FB/HP-β-CD inclusion complex (d).

3.2. Preparation of DMNs

The mechanical strength of DMNs is critical for efficient drug delivery.[41] Using the drug-cyclodextrin inclusion complex alone as the microneedle tip material often leads to high hygroscopicity, which can compromise the mechanical stability of the microneedles. Here we fabricated biphasic DMNs carrying FB/HP-β-CD inclusion complexes using a mold casting method. The microneedle tips were formulated as shown in Table 1, whereas the backing layer was formed *via* photopolymerization. The microneedle tip formulations F1, F2, and F3, which contained a viscous polymer solution of PVP K90, PVA 05-88, chondroitin sulfate, and FB/HP-β-CD inclusion complex, showed poor mold filling and low tip yields. The drug loading content of each formulation was determined and found to be 2.22 ± 0.07 mg for F1, 2.50 ± 0.14 mg for F2, 2.18 ± 0.03 mg for F3, and 2.67 ± 0.11 mg for F4. Among them, F4 exhibited the highest drug content. Considering both mechanical strength and drug loading efficiency, subsequent *ex vivo* characterization and *in vivo* pharmacokinetic studies were carried out using formulation F4.

First, the microneedle morphology was assessed using SEM analysis. As shown in Fig. 2, an array of smooth conical microneedles with a tip height of 760 μm were observed. The tip height was slightly shorter than the mold height of 780 μm due to drying induced shrinkage during the fabrication.[42] All needles were uniform in shape without bending or breakage. Next, the drug distribution within the microneedles was visualized using confocal imaging analysis (Fig. 3). RhB red fluorescence dye was loaded into microneedle tips to simulate the localization of drugs, while Cou-6 green fluorescence dye was incorporated into the backing layer. The 3D images produced from z-scan sections of the microneedles confirmed that the tip height calculated from confocal images was consistent with that derived from SEM analysis; and no evidence of drug migration from the tips into the backing layer was observed.

Furthermore, we analyzed the total drug load that can be delivered by 1 cm² of biphasic FB DMN patch. Results from HPLC measurements showed that each biphasic DMN patch has a FB loading capacity of 2.67 ± 0.11 mg per 1 cm² ($n = 3$), which significantly surpasses the loading capacity of

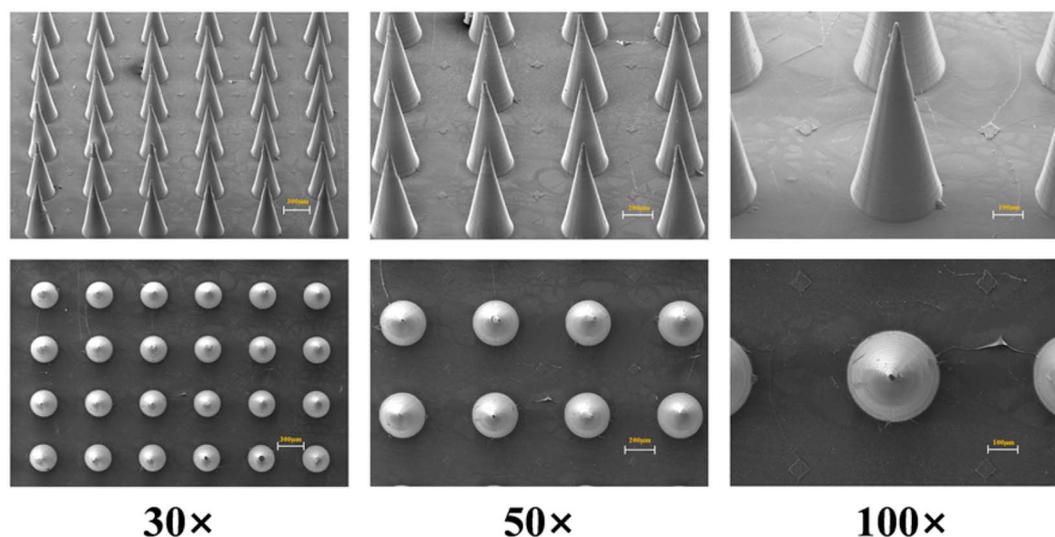**Fig. 2** SEM images of needle tips at different magnifications (30×, 50×, 100×). Top row: front view; and bottom row: top-down view.
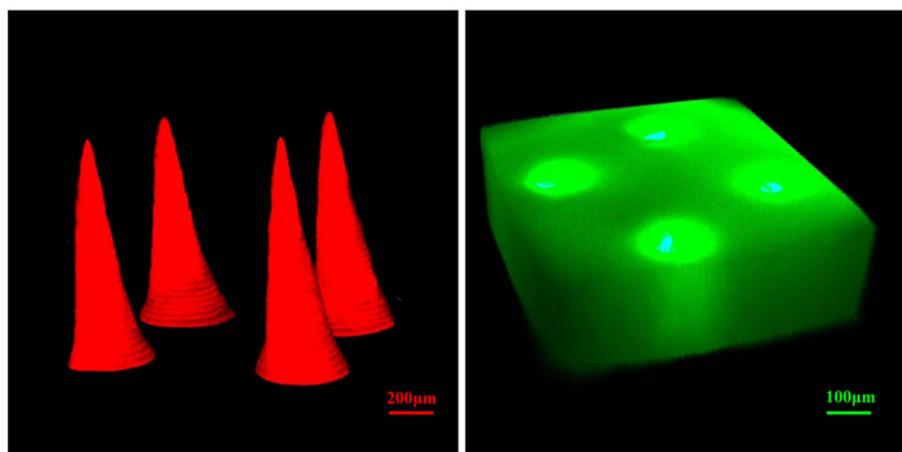
Fig. 3 Microneedles fabricated with tips loaded with RhB (red) and Cou-6 containing PS backing material (green) were subjected to confocal microscopy analysis. Images showing 3D reconstruction of the microneedle tip (left) and the backing layer (right).

conventional microneedles, typically ranging from tens to hundreds of micrograms.[43] Moreover, this delivery capacity per unit area is approximately ten times higher than the drug load of commercially available flurbiprofen gel patches (40 mg per 13.6 cm × 10 cm).[44] The significant enhancement in drug loading underscores the primary advantage of biphasic DMNs, achieving superior drug delivery efficiency within a smaller application area. This suggests their potential as a more efficient and convenient alternative to conventional transdermal delivery systems.

3.3. Mechanical strength and insertion capability of microneedles

To ensure successful application, the microneedle tips must possess sufficient mechanical strength to overcome the inherent elasticity of the skin.[45,46] Previous studies have reported that the total force applied to a microneedle array during skin insertion is typically on the order of several newtons (approximately 3 N).[47] To examine the mechanical strength of microneedles fabricated in our study, we conducted insertion tests using 8 layers of Parafilm as a skin simulant. By applying a force of 4 N, microneedles fabricated with F4 formulation were able to penetrate through the 5th layer of Parafilm whereas other microneedles penetrated up to 3 layers (Fig. 4A). The force–displacement curve indicated that a single F4 microneedle can withstand a force of 0.58 ± 0.10 N, which is higher than the force required to penetrate the skin (ranging from 0.1–2 N)[48,49] (Fig. 4B). The superior insertion capability of F4 microneedles suggests that they are more likely to achieve consistent and reliable transdermal drug administration *in vivo*. Additionally, the increased mechanical robustness may reduce the risk of microneedle breakage during application, enhancing patient safety and user experience.
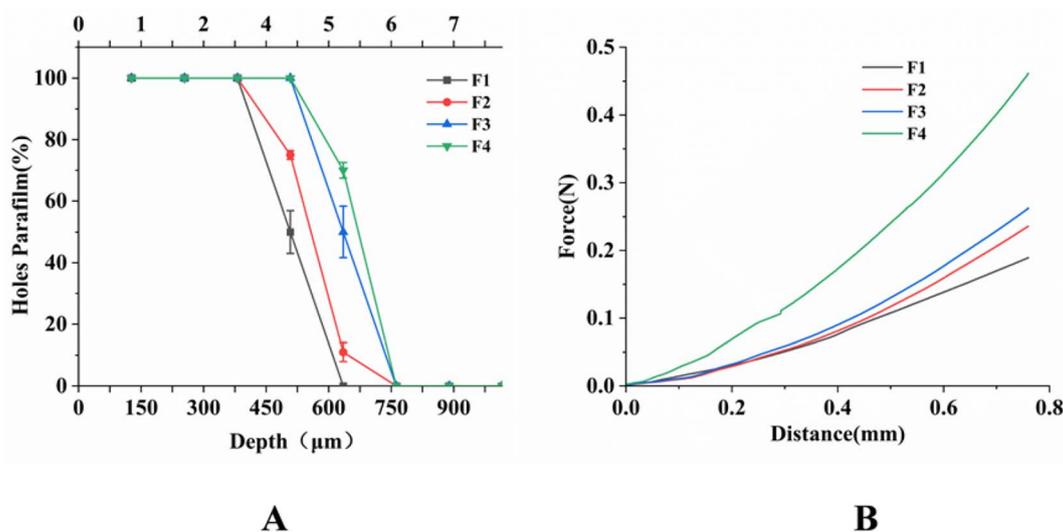

A

B

Fig. 4 The insertion rate of microneedles into Parafilm. (A) Microneedles fabricated from F1–F4 formulations were tested and the insertion depth was estimated based on the number of Parafilm layers penetrated. Data represent mean ± S.D. (*n* = 3). (B) The force–displacement curve of the microneedles.
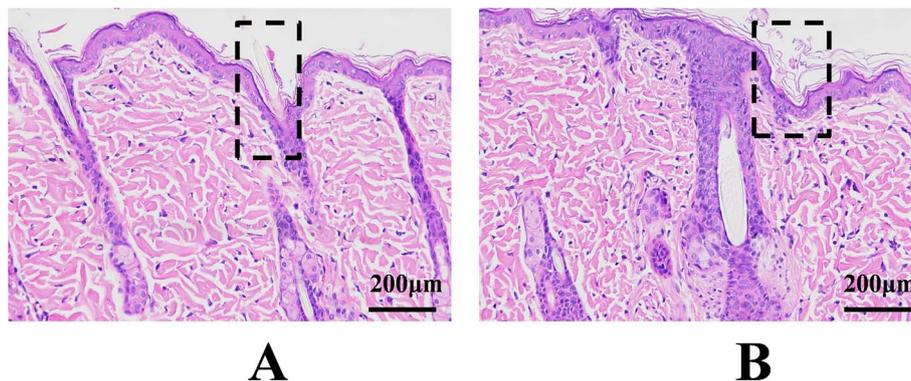
Fig. 5 Histological analysis of rat skin tissue sections at 10 min (A) and 2 h (B) after microneedle application. Scale bar = 200 μm.

In addition, the ability of microneedles to penetrate skin was tested in rats. The histology analysis of rat skin showed that the penetration depth was 450 μm following F4 microneedle application (Fig. 5A). Importantly, the skin puncture holes were healed after 2 hours (Fig. 5B). Taken together, the microneedles produced in our study demonstrated sufficient mechanical strength needed for delivering drugs through the skin.

3.4. *Ex vivo* transdermal permeation results

To evaluate the effect of different backing materials on drug delivery efficiency, we fabricated FB/HP-β-CD inclusion complex DMN tips using formulation F4 in conjunction with soluble or insoluble backing (SI Tables S3 and S4). *Ex vivo* permeation profiles were determined using Franz diffusion cells with rat skin and PBS (pH 7.4) as the receptor medium at 37 °C. As shown in Fig. 6 the cumulative drug release of DMNs with insoluble backing was approximately twice that of those with soluble backing within 4 h of application. After 24 h, nearly $95.90 \pm 3.59\%$ of FB permeated across the skin from the DMNs with insoluble backing, whereas only $53.45 \pm 4.74\%$ permeated
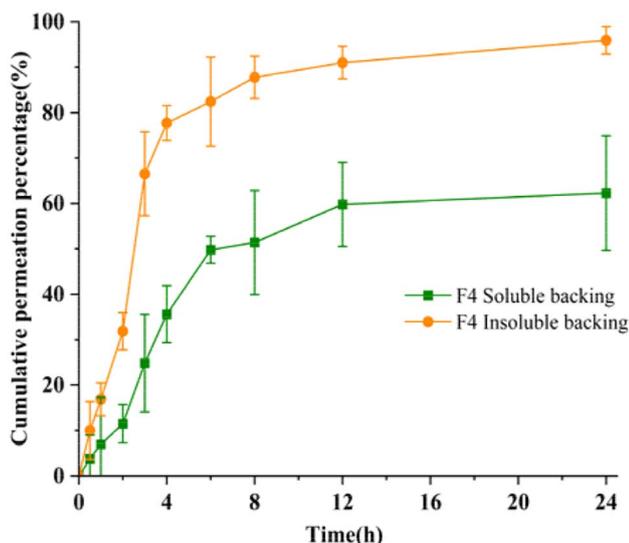

Fig. 6 *Ex vivo* transdermal permeation profiles of FB/HP-β-CD complex DMNs with soluble or insoluble backing (Mean ± S.D., $n = 3$).

from those with soluble backing. In addition, the microneedle tips dissolved and separated quickly from the insoluble backing layer upon insertion, potentially minimizing skin irritation. Thus, the biphasic DMNs with insoluble backing produced in our study provide a more efficient delivery system.

To further elucidate the underlying release mechanisms contributing to these differences, the cumulative permeation data were fitted to four common kinetic models: zero-order, first-order, Higuchi, and Korsmeyer–Peppas.[50,51] Of these models, the Higuchi model exhibited the highest correlation coefficients ($R^2 = 0.991$ for insoluble backing and 0.982 for soluble backing), indicating a predominantly diffusion-controlled release process. However, for mechanistic interpretation, the Korsmeyer–Peppas model was applied, as it enables distinction between Fickian and non-Fickian transport *via* the diffusion exponent (n). The detailed fitting parameters for each model are summarized in SI Table S6.

The fitted n value of 0.489 for DMNs with an insoluble backing suggests Fickian diffusion, which is consistent with a release mechanism governed by passive diffusion. This device design restricts drug migration toward the backing to ensure unidirectional release into the skin, thereby resulting in a uniform profile and high delivery efficiency. In contrast, DMNs with a soluble backing exhibited an n value of 0.612, indicative of non-Fickian transport. HPLC analysis of the residual backing layer post-application confirmed that approximately 25% of the drug was retained due to partial dissolution and migration. This significant retention directly accounts for the anomalous release behavior and the suboptimal delivery efficiency.

3.5. *In vivo* pharmacokinetic studies

To evaluate the drug delivery performance of the biphasic inclusion complex-based dissolving microneedle system, FB was employed as a model drug in both single- and multiple-dose pharmacokinetic studies. A commercial FB gel patch was used as the reference formulation. In the single-dose study (Fig. 7A), biphasic DMNs achieved a peak plasma concentration (C_{max}) of 124.4 ± 11.4 μg mL^{-1} within 2 h, which was 5.53-fold higher than that of the commercial patch (22.5 ± 2.6 μg mL^{-1}, $T_{max} = 8$ h). The AUC$_{0\rightarrow24h}$ of DMNs (1247.6 ± 240.7 μg h mL^{-1})
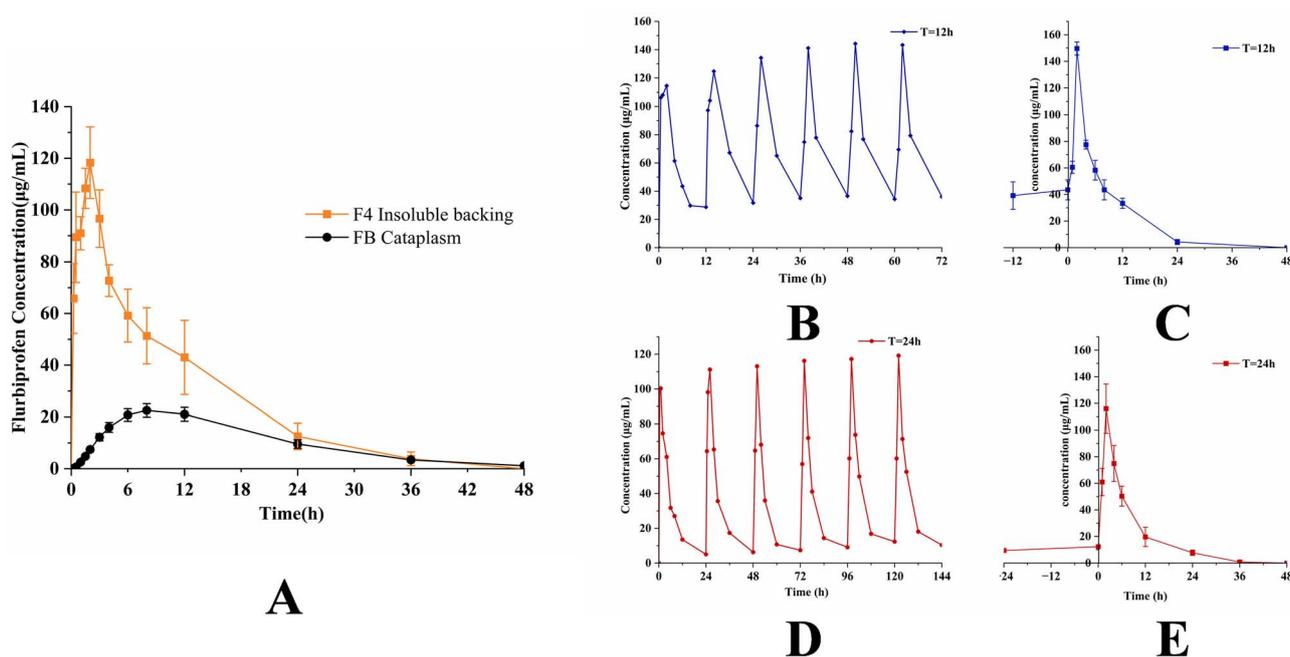
Fig. 7 The plasma concentrations of FB following single and multiple dosing regimens in rats. The FB concentrations in the plasma at different time points were measured following a single administration of biphasic DMN patches (A) or multiple dosing with time interval of $\tau = 12$ h (B–C) and time interval of $\tau = 24$ h (D and E). (Mean $\pm$ S.D., $n = 6$).

was 2.57-fold greater than that of the patch (485.0 $\pm$ 63.0 µg h mL^{-1}) (Table 3). Furthermore, the plasma concentration of the DMN group remained consistently above that of the patch group throughout the 24 hours period.

The improved pharmacokinetic performance observed with the biphasic DMN system can be attributed to its fundamental delivery advantage. Physical insertion of the microneedle tips creates micron-scale channels in the skin, allowing rapid dissolution of the drug-loaded matrix directly within the dermal interstitial fluid, which is rich in blood and lymphatic vessels.[52] In contrast, drug absorption from the gel patch relies on passive diffusion across multiple skin barriers, during which absorption and elimination occur simultaneously, resulting in delayed T_{max} and reduced systemic exposure. The higher AUC observed for the DMN group therefore reflects its superior delivery efficiency and improved bioavailability.[53]

In contrast to most studies that focus solely on single-dose administration, we further explored the pharmacokinetics of the biphasic DMN system in multiple-dose administration. To better simulate clinical dosing strategies and benchmark against the commercial flurbiprofen gel patch, two dosing regimens were selected, including once daily (24 hours interval) and twice daily (12 hours interval), which correspond to the typical usage of one or two patches per day.[5] Following

administration of three consecutive doses, both regimens achieved steady-state plasma concentrations (Fig. 7B–E). The twice-daily regimen yielded an average steady-state concentration (C_{av}) of 65.8 $\pm$ 8.8 µg mL^{-1} and a total exposure (AUC$_{ss}$) of 789.3 $\pm$ 88.0 µg h mL^{-1}, whereas the once-daily regimen resulted in a C_{av} of 33.2 $\pm$ 3.3 µg mL^{-1} with a comparable AUC$_{ss}$ of 797.0 $\pm$ 78.5 µg h mL^{-1}. The similar AUC$_{ss}$ values indicate consistent total drug delivery across the different dosing intervals. Notably, plasma drug concentrations declined to undetectable levels within 48 hours after the final administration in both regimens, suggesting low risk of systemic accumulation.

The comparable AUC$_{ss}$ between the two multiple-dose regimens, despite differing fluctuation patterns, demonstrates consistent total drug delivery, which can be flexibly modulated by the dosing interval. The absence of drug accumulation confirms the pharmacokinetic safety of this formulation. In direct comparison with a commercially available product, the biphasic DMN system developed in this study systematically demonstrates its advantages of rapid onset and enhanced bioavailability following a single dose. This work provides strong support for overcoming key challenges in the clinical translation of microneedle technology, namely insufficient drug loading and the lack of comprehensive comparative studies.

Table 3 Pharmacokinetic parameters of single-dose administration (Mean $\pm$ S.D., $n = 6$)

Pharmacokinetic parameters	T_{max} (h)	C_{max} (µg mL^{-1})	AUC$_{0 \to 24h}$ (µg h mL^{-1})	$T_{1/2}$ (h)	CL (mL h^{-1} kg)	MRT$_{0 \to 24h}$ (h)
F4 MN	2.0	124.4 $\pm$ 11.4	1247.6 $\pm$ 240.7	7.6 $\pm$ 1.4	9.1 $\pm$ 0.2	9.0 $\pm$ 1.5
FB cataplasms	8.0	22.5 $\pm$ 2.6	485.0 $\pm$ 63.0	22.6 $\pm$ 1.9	3.0 $\pm$ 0.1	15.4 $\pm$ 0.6

4. Discussion

In the development of dissolving microneedles, the choice of matrix material is fundamental for achieving high drug loading and effective transdermal delivery.[54,55] Cyclodextrin enhances the mechanical strength and flexibility of the microneedles through multiple supramolecular interactions, including host-guest recognition and hydrogen bonding networks.[56–58] Its relatively low molecular weight also facilitates rapid dissolution in the skin, enhancing drug release rate and bioavailability. These characteristics collectively suggest that cyclodextrin holds substantial potential as a matrix material for microneedles. Compared to traditional microneedle materials (*e.g.*, hyaluronic acid, gelatin), HP-β-CD, with its unique amphiphilic cavity structure, can form inclusion complexes with FB, significantly enhancing the apparent solubility of the drug. This property lays the foundation for achieving milligram-level drug loading within the limited space of microneedles.[59]

However, the use of cyclodextrin as a sole matrix material for microneedles presents limitations. Due to strong intermolecular interactions,[60] cyclodextrin-based microneedles are prone to hygroscopicity during storage, leading to reduced mechanical strength and impaired insertion capability, which imposes stricter storage requirements. To address this, in the initial formulation screening, we incorporated polymers such as PVA 05-88, HPMC E5, chondroitin sulfate and PVP K90 along with cyclodextrin to enhance matrix properties. These polymers were selected based on their film-forming and adhesive properties.[61–64] Results from our assessments of microneedle morphology, mechanical strength, and drug loading capacity demonstrated that the microneedles with an HPMC-based matrix achieved the optimal balance between mechanical strength and drug loading, thus making it the most suitable choice for enhancing the structural stability of cyclodextrin-based microneedle system.

Beyond the intrinsic properties of the matrix, the compatibility between the drug and cyclodextrin also plays a critical role in determining the efficacy of microneedle-based delivery systems. In this study, FB, a small-molecule model drug, was selected to form an inclusion complex with hydroxypropyl-β-cyclodextrin, validating the drug-loading and release capabilities of the system. However, considering the diversity in molecular structure, polarity, and steric hindrance across different drug molecules, a single model drug is insufficient to comprehensively evaluate the applicability of this system. Previous studies have indicated that other CD derivatives, such as sulfobutyl ether-β-cyclodextrin (SBE-β-CD), may offer superior inclusion efficiency and solubilization capacity.[65] Therefore, future work should focus on the systematic screening of various CD derivatives in combination with drugs of diverse physicochemical properties, in order to evaluate the versatility and efficiency of this microneedle platform in delivering macromolecular and biological therapeutics.

Moreover, our pharmacokinetic studies confirmed the design advantages of the inclusion complex biphasic microneedles. Following a single dose, plasma concentrations rapidly peaked within 2 hours (T_{max}), much faster than the 8 hours T_{max} observed with commercial patches, reflecting the rapid dissolution and absorption of the drug from the microneedle tips. This rapid onset of action is primarily attributed to the biphasic microneedles, which deposit a high concentration of the FB/HP-β-CD inclusion complex directly in the dermis. The drug is quickly released in the interstitial fluid and enters systemic circulation through capillaries. Furthermore, the DMN group showed an $AUC_{0 \rightarrow 24h}$ that was 2.57 times of the commercial patch, demonstrating that the combination of "inclusion solubilization" and "biphasic microneedles" successfully increased both the drug loading and delivery efficiency of a poorly soluble drug. The results from the multiple-dose study further demonstrated the translational potential of this system. By adjusting the dosing interval (12 hours *vs.* 24 hours), we were able to modulate steady-state plasma drug concentrations to potentially meet the therapeutic needs for acute pain flare-ups or chronic symptom maintenance. While the system favors rapid drug release, the drug is also quickly cleared from the system after cessation of dosing, thus minimizing safety concerns. This feature makes it particularly suitable for managing acute symptoms such as postoperative pain.

Although this study demonstrated the potential of phase-separated inclusion complex microneedles in enhancing drug delivery efficiency, the *in vivo* behavior and mechanistic pathways associated with their clinical application remain insufficiently understood. Upon application, the microneedle tips are the first to interact with the skin, and their dissolution behavior directly influences both the rate and site of drug release, ultimately determining whether the drug can effectively penetrate the stratum corneum and enter systemic circulation. To date, limited research has systematically elucidated the dissolution kinetics of such microneedles within skin tissue, the stability of inclusion complexes under physiological conditions, or the complete pathway of transdermal absorption into the bloodstream. Key factors such as the dissolution rate and depth of the microneedle tips, and their interactions with skin microstructures, may critically influence overall delivery performance. Consequently, future studies should aim to establish a robust *in vitro–in vivo* correlation (IVIVC) model by bridging *in vitro* release profiles with *in vivo* absorption behavior, thereby enabling a deeper understanding of the release and absorption mechanisms of inclusion complex microneedles and supporting their clinical translation.

5. Conclusion

This study addresses key challenges in the transdermal delivery of poorly soluble drugs using dissolving microneedle systems. By integrating cyclodextrin inclusion technology with a biphasic DMN design, flurbiprofen was successfully formulated into a system that improves drug solubility and enhances transdermal delivery efficiency. Pharmacokinetic evaluation demonstrated faster systemic absorption and higher bioavailability compared with a commercial gel patch. In addition, the biphasic design enables flexible modulation of dosing profiles,

which may be advantageous for meeting different therapeutic requirements.

Several limitations should be acknowledged. First, flurbiprofen was used as a single model drug, and further studies are required to verify the applicability of this platform to other poorly soluble drugs with diverse physicochemical properties. Second, the preparation of the inclusion complex involves lyophilization, which may introduce challenges related to production cost and. Future work will focus on optimizing the microneedle matrix to incorporate controlled-release properties to expand its application in long-term treatment of chronic diseases and developing robust IVIVC models to accelerate formulation screening and clinical translation. Overall, this study not only provides an efficient DMN platform for the delivery of poorly soluble drugs but also demonstrates a feasible pathway for translating microneedle technology into clinical practice.

Conflicts of interest

The authors declare no conflict of interest.

Data availability

The data supporting this article are included within the main text or the supplementary information (SI). Supplementary information: additional figures and tables, including phase solubility data (Fig. S1), schematic comparison of microneedle designs (Fig. S2), orthogonal experimental design details and results (Tables S1 and S2), backing layer formulations (Tables S3 and S4), ANOVA statistical analysis (Table S5), and drug release kinetic model parameters (Table S6). See DOI: https://doi.org/10.1039/d5ra08424e.

Acknowledgements

References

1 S. Henry, D. V. McAllister, M. G. Allen and M. R. Prausnitz, *J. Pharm. Sci.*, 1998, **87**, 922–925.

2 Á. Cárcamo-Martínez, B. Mallon, J. Domínguez-Robles, L. K. Vora, Q. K. Anjani and R. F. Donnelly, *Int. J. Pharm.*, 2021, **599**, 120455.

3 N. Tariq, M. W. Ashraf and S. Tayyaba, *J. Pharm. Innov.*, 2022, **17**, 1464–1483.

4 T. N. Tarbox, A. B. Watts, Z. Cui and R. O. Williams, *Drug Deliv. Transl. Re.*, 2018, **8**, 1828–1843.

5 M. Ali, S. Namjoshi, H. A. E. Benson, Y. Mohammed and T. Kumeria, *J. Controlled Release*, 2022, **347**, 561–589.

6 Y. Wu, Z. Tang, S. Ma and L. Du, *J. Pharm. Pharmacol.*, 2023, **75**, 1011–1020.

7 F. Moawad, R. Pouliot and D. Brambilla, *J. Controlled Release*, 2025, **383**, 113794.

8 S. P. Sullivan, D. G. Koutsonanos, M. del Pilar Martin, J. W. Lee, V. Zarnitsyn, S.-O. Choi, N. Murthy, R. W. Compans, I. Skountzou and M. R. Prausnitz, *Nat. Med.*, 2010, **16**, 915–920.

9 N. G. Rouphael, M. Paine, R. Mosley, S. Henry, D. V. McAllister, H. Kalluri, W. Pewin, P. M. Frew, T. Yu, N. J. Thornburg, S. Kabbani, L. Lai, E. V. Vassilieva, I. Skountzou, R. W. Compans, M. J. Mulligan, M. R. Prausnitz, A. Beck, S. Edupuganti, S. Heeke, C. Kelley and W. Nesheim, *The Lancet*, 2017, **390**, 649–658.

10 T. Phoka, N. Wanichwecharungruang, N. Dueanphen, N. Thanuthanakhun, P. Kietdumrongwong, A. Leelahavanichkul and S. Wanichwecharungruang, *J. Pharm. Sci.*, 2024, **113**, 2734–2743.

11 C. I. Tobos and K. A. Woodrow, *Acta Biomater.*, 2025, **200**, 115–131.

12 H. X. Nguyen, B. N. Tran, H. T. Nguyen, V. S. Nguyen and C. N. Nguyen, *J. Drug Delivery Sci. Technol.*, 2025, **114**, 107422.

13 L. Y. Chu, S. O. Choi and M. R. Prausnitz, *J. Pharm. Sci.*, 2010, **99**, 4228–4238.

14 D. D. Zhu, X. P. Zhang, C. B. Shen, Y. Cui and X. D. Guo, *Drug Delivery Transl. Res.*, 2019, **9**, 1133–1142.

15 A. J. Paredes, P. E. McKenna, I. K. Ramöller, Y. A. Naser, F. VolpeZanutto, L. Mingshan, M. Abbate, Z. Li, Z. Chunyang, J. M. AbuErshaid, D. Xianbing and R. F. Donnelly, *Adv. Funct. Mater.*, 2020, **31**, 2005792.

16 S. S. Yerneni, E. P. Yalcintas, J. D. Smith, S. Averick, P. G. Campbell and O. B. Ozdoganlar, *Acta Biomater.*, 2022, **149**, 198–212.

17 C. Jiaxin, L. Yang, Q. Zhenzhen, T. Xiaosheng, C. K. Subhas and L. Shenzhou, *J. Drug Delivery Sci. Technol.*, 2022, **74**, 103611.

18 Z. Jan, M. Mohammadi, S. Mollazadeh, K. Abnous, S. M. Taghdisi, A. Danesh, M. Ramezani and M. Alibolandi, *J. Drug Delivery Sci. Technol.*, 2025, **111**, 107128.

19 Q. Wanbing, Q. Guilan, S. Ying, C. Minglong, Y. Peipei, F. Disang, W. Ting, H. Xinyu, P. Xin and W. Chuanbin, *Theranostics*, 2020, **10**, 8179–8196.

20 Y. Wendong, Y. Xingxing, X. Xianze, F. Qiaomei, S. Yujun, Z. Shanshan, S. Zheng and X. Hairu, *Biomed. Pharmacother.*, 2024, **178**, 117219.

21 S. Li, D. Xia and M. R. Prausnitz, *Adv. Funct. Mater.*, 2021, **31**, 2103359.

22 S. Deng, Y. Shuai, S. Zhang, C. Sun, L. Chang, J. Xu, L. Tong, Q. Ji, M. Li, J. Dai and Y. Ju, *Biomater. Sci.*, 2023, **11**, 5605–5617.

23 N. Ismayilzada, C. Tarar, S. R. Dabbagh, B. K. Tokyay, S. A. Dilmani, E. Sokullu, H. E. Abaci and S. Tasoglu, *Biofabrication*, 2024, 16.

24 R. Ge, C. Sun, J. Su, M. Tian, Y. Qiao, J. Li, J. Du, W. Wei, S. Yang, C. Wu, Q. Xiang, Y. Xing and H. Dong, *Anal. Chem.*, 2024, **96**, 2799–2809.

25 E. Tunçel, S. Tort, S. Han, Ç. Yücel and F. Tırnaksız, *Drug Delivery Transl. Res.*, 2025, **15**, 2116–2145.

26 J. Zhang, H. Li, L. Albakr, Y. Zhang, A. Lu, W. Chen, T. Shao, L. Zhu, H. Yuan, G. Yang, N. J. Wheate, L. Kang and C. Wu, *J. Controlled Release*, 2023, **360**, 687–704.

27 K. Chaturvedi, K. Ganguly, A. R. Kulkarni, M. N. Nadagouda, J. Stowbridge, W. E. Rudzinski and T. M. Aminabhavi, *RSC Adv.*, 2013, **3**, 7064–7070.

28 H. Bera, S. Chekuri, S. Sarkar, S. Kumar, N. B. Muvva, S. Mothe and J. Nadimpalli, *J. Mol. Liq.*, 2016, **215**, 135–143.

29 C. K. Reddy, E. S. Jung, S. Y. Son and C. H. Lee, *LWT–Food Sci. Technol.*, 2020, **131**, 109723.

30 Z. Li, H. Liu, C. Qi, A. Yang, S. Deng and J. Inclusion Phenom, *Macrocyclic Chem.*, 2019, **93**, 289–299.

31 B. G. Prajapati, L. F. Alzaghari, P. Alam, M. Fareed and D. U. Kapoor, *J. Drug Delivery Sci. Technol.*, 2025, **107**, 106818.

32 E. Larrañeta, J. Moore, E. M. Vicente-Pérez, P. González-Vázquez, R. Lutton, A. D. Woolfson and R. F. Donnelly, *Int. J. Pharm.*, 2014, **472**, 65–73.

33 Y. Yang, W. Song, N. Wang, Y. Ren and H. Liu, *Biomater. Adv.*, 2022, **135**, 212729.

34 Y. Kim, S. A. Bhattaccharjee, M. Beck-Broichsitter and A. K. Banga, *Biomed. Microdevices*, 2019, **21**, 104.

35 T. Hatanaka, E. Manabe, K. Sugibayashi and Y. Morimoto, *Pharm. Res.*, 1994, **11**, 654–658.

36 E. E. M. Eid, A. A. Almaiman, S. A. Alshehade, W. Alsalemi, S. Kamran, F. O. Suliman and M. A. Alshawsh, *Molecules*, 2023, **28**, 4096–4115.

37 D. Kabirov, T. Silvestri, M. Niccoli, T. Usacheva, L. Mayol, M. Biondi and C. Giancola, *J. Therm. Anal. Calorim.*, 2022, **147**, 347–353.

38 T. Loftsson and M. E. Brewster, *J. Pharm. Sci.*, 2012, **101**, 3019–3032.

39 S. Melo-Guímaro, R. Cardoso, C. S. Lobo, D. A. Pereira, C. Varela, J. Santos, C. P. João, C. Serpa and L. G. Arnaut, *Eur. J. Pharm. Biopharm.*, 2024, **202**, 114390.

40 A. Conde Penedo, V. Díaz Tomé, A. Fernández Ferreiro, M. González Barcia and F. J. Otero Espinar, *Eur. J. Pharm. Biopharm.*, 2021, **162**, 12–22.

41 L. K. Vora, A. J. Courtenay, I. A. Tekko, E. Larrañeta and R. F. Donnelly, *Int. J. Biol. Macromol.*, 2020, **146**, 290–298.

42 J. Mönkäre, M. Reza Nejadnik, K. Baccouche, S. Romeijn, W. Jiskoot and J. A. Bouwstra, *J. Controlled Release*, 2015, **218**, 53–62.

43 S. P. Sullivan, N. Murthy and M. R. Prausnitz, *Adv. Mater.*, 2008, **20**, 933–938.

44 M. Martens, *Clin. Rheumatol.*, 1997, **16**, 25–31.

45 G. Bonfante, H. Lee, L. Bao, J. Park, N. Takama and B. Kim, *Micro Nano Syst. Lett.*, 2020, **8**, 13.

46 S. A. Ranamukhaarachchi and B. Stoeber, *Biomed. Microdevices*, 2019, **21**, 100.

47 A. Ripolin, J. Quinn, E. Larrañeta, E. M. Vicente-Perez, J. Barry and R. F. Donnelly, *Int. J. Pharm.*, 2017, **521**, 92–101.

48 H. Kalluri and A. K. Banga, *J. Drug Delivery Sci. Technol.*, 2009, **19**, 303–310.

49 S. P. Davis, B. J. Landis, Z. H. Adams, M. G. Allen and M. R. Prausnitz, *J. Biomech.*, 2004, **37**, 1155–1163.

50 Y.-J. Oh, N.-W. Kang, H.-R. Jeong, S.-Y. Sohn, Y.-E. Jeon, N.-Y. Yu, Y. Hwang, S. Kim, D.-D. Kim and J.-H. Park, *Pharm. Res.*, 2022, **39**, 989–999.

51 Z. N. Zafar, A. Mahmood, R. M. Sarfraz and A. Elaissari, *Micromachines*, 2022, **13**, 1304.

52 C. Wu, Q. Yu, C. Huang, F. Li, L. Zhang and D. Zhu, *Acta Pharm. Sin. B*, 2024, **14**, 5161–5180.

53 I. Yataba, N. Otsuka, I. Matsushita, M. Kamezawa, I. Yamada, S. Sasaki, K. Uebaba, H. Matsumoto and Y. Hoshino, *Eur. J. Clin. Pharmacol.*, 2016, **72**, 53–59.

54 A. Bocchino, C. Marquez-Grana, O. P. Singh, E. Melnik, S. Kurzhals, G. C. Mutinati, S. Coulman, C. Martin, K. W. Ng, M. Massufero Vergilio, J. Birchall, P. Donovan, P. Galvin and C. O'Mahony, *Sens. Actuators, A*, 2025, **388**, 116491.

55 R. Ali, P. Mehta, M. S. Arshad, I. Kucuk, M. W. Chang and Z. Ahmad, *AAPS PharmSciTech*, 2019, **21**, 12.

56 G. Fang, X. Yang, S. Chen, Q. Wang, A. Zhang and B. Tang, *Coord. Chem. Rev.*, 2022, **454**, 214352.

57 K. M. Sahu, S. Patra and S. K. Swain, *Int. J. Biol. Macromol.*, 2023, **240**, 124338.

58 T. Loftsson, P. Saokham and A. R. Sá Couto, *Int. J. Pharm.*, 2019, **560**, 228–234.

59 D. U. Kapoor, R. Garg, P. K. Saini, M. Gaur and B. G. Prajapati, *Nano-Struct. Nano-Objects*, 2024, **40**, 101358.

60 H. Wang, Y. Fu, J. Mao, H. Jiang, S. Du, P. Liu, J. Tao, L. Zhang and J. Zhu, *Adv. Mater.*, 2022, **34**, e2207832.

61 Q. Yan, J. Weng, S. Shen, Y. Wang, M. Fang, G. Zheng, Q. Yang and G. Yang, *Polymers*, 2021, **13**, 3043.

62 A. Cheng, S. Wentao, X. Mengzhen, Z. Suohui and Y. Gao, *Int. J. Polym. Mater. Polym. Biomater.*, 2022, **71**, 72–78.

63 P. W. R. Ananda, D. Elim, H. S. Zaman, W. Muslimin, M. G. R. Tunggeng and A. D. Permana, *Int. J. Pharm.*, 2021, **609**, 121204.

64 M. A. S. Abourehab, S. Baisakhiya, A. Aggarwal, A. Singh, M. A. Abdelgawad, A. Deepak, M. J. Ansari and S. Pramanik, *J. Mater. Chem. B*, 2022, **10**, 9125–9178.

65 H. Sadaquat, M. Akhtar and J. Inclusion Phenom, *Macrocyclic Chem.*, 2020, **96**, 333–351.